

Energy density in density functional theory: Application to crystalline defects and surfacesMin Yu,¹ Dallas R. Trinkle,^{2,*} and Richard M. Martin¹¹*Department of Physics, University of Illinois at Urbana-Champaign, Urbana, Illinois 61801, USA*²*Department of Materials Science and Engineering, University of Illinois at Urbana-Champaign, Urbana, Illinois 61801, USA*

(Received 21 November 2010; published 8 March 2011)

We propose a method for decomposing the total energy of a supercell containing defects into contributions of individual atoms, using the energy density formalism within the density functional theory. The spatial energy density is unique up to a gauge transformation, and we show that unique atomic energies can be calculated by integrating over Bader and charge-neutral volumes for each atom. Numerically, we implement the energy density method in the framework of the Vienna *ab initio* simulation package (VASP) for both norm-conserving and ultrasoft pseudopotentials and the projector augmented-wave method, and we use a weighted integration algorithm to integrate the volumes. Surface energies and point defect energies can be calculated by integrating the energy density over the surface region and the defect region, respectively. We compute energies for several surfaces and defects: the (110) surface energy of GaAs, the monovacancy formation energies of Si, the (100) surface energy of Au, and the interstitial formation energy of O in a hexagonal close-packed Ti crystal. The surface and defect energies calculated using our method agree with size-converged calculations of the difference in the total energies of a system with versus a system without defects. Moreover, the convergence of the defect energies with size can be found from a *single* calculation.

DOI: [10.1103/PhysRevB.83.115113](https://doi.org/10.1103/PhysRevB.83.115113)

PACS number(s): 74.20.Pq, 74.25.Bt, 61.72.S–

I. INTRODUCTION

Total energy is one of the most important quantities in a solid-state system, as it determines the stable configuration, and its derivatives provide other equilibrium properties. The assignment of energy to particular finite volumes can provide additional detailed information, such as defect formation energies. For example, the surface energy of a given facet of a crystal is meaningful for predicting the equilibrium crystal shape and preferred crystal growth directions, and should depend only on the properties of the surface. The formation energy of a point defect is important to understand phase stability and should depend only on the properties in the vicinity of the defect. However, density functional theory (DFT) calculations¹ provide only the total energy for a given configuration, not a spatial partitioning of energy into additive contributions—instead, defect energies are determined as a difference of two or more separate total energy calculations.

The energy density method² can provide the formation energies for more than one point defect, surface, or interface in a single calculation, as well as a picture of the distribution of the energy among the surrounding atoms. The energy density formula derived by Chetty and Martin is a reciprocal-space expression for norm-conserving pseudopotential³ (NCPP) with the local density approximation^{4,5} (LDA), where the ion-ion interaction is treated in a similar manner as the Ewald sum.⁶ The energy density is not unique since there are multiple definitions of the kinetic and Coulomb energy densities that integrate to the same well-defined total energy. The different definitions can be considered as gauge variability; defining a unique gauge-independent energy requires the identification of spatial volumes where the gauge differences integrate to 0. Chetty and Martin^{2,7} showed that the surface energy for a crystal can be calculated by an integral over a region to high-symmetry planes within the bulk of the crystal, where symmetry ensures that the gauge dependent terms integrate to 0. Therefore, two polar surface energies such as the (111)

and the ($\bar{1}\bar{1}\bar{1}$) surfaces of a zincblende semiconductor GaAs can be integrated independently in a single calculation. This compares with more complex approaches that use multiple wedge geometries to extract polar surface energies for specific geometries.⁸ Rapcewicz *et al.*⁹ followed the energy density formalism but generalized the method to low-symmetry system such as the (0001) surface of GaN and the (0001) surface of SiC by introducing Voronoi polyhedra for the integration volumes; however, it should be noted that Voronoi polyhedra are gauge-independent integration volumes only in specific situations. Ramprasad¹⁰ extended the application of energy density method from surfaces to point defects of metals and presented two applications on the monovacancy of Al and the (001) surface of Al.

We reformulate the expression of the real-space energy density for the projector-augmented wave¹¹ (PAW) method and norm-conserving and ultrasoft pseudopotentials¹² (USPP), grouping terms in a similar manner. We implement the energy density method in the Vienna *ab initio* simulation package^{13,14} (VASP). We also demonstrate the usefulness of assigning an energy to each atom using gauge-independent integration volumes. Excluding cases that can be determined by symmetry—such as the energy of an atom in the diamond structure that is half the total energy of a unit cell—the assignment is not unique. Nevertheless, there are two primary reasons for developing an approach based on gauge-independent volumes. One advantage is that it provides an automatic procedure to choose volumes that do not depend on the choices of planes or polyhedra in the calculations mentioned above. The resulting surface and defect energies are the same as for the special cases above but can also be used for general cases. In addition, the energy per atom partitions space to individual defect regions and provides a measure of finite-size errors in a single calculation. Moreover, within an individual defect—for example, a vacancy in silicon—the atomic energy shows the contribution of individual atomic relaxations to the

total formation energy, which can be useful for understanding changes to the stability of individual defects and surfaces.

The assignment of energy to an atom derives from Bader's "atoms in molecules" theory.¹⁵ Although our work is different, one element is the same: the calculation of volume around each atom where the kinetic energy is unique. We extend this to find a charge neutral volume for a unique classical Coulomb energy. In Bader's work, a local form of virial theorem relates the local electron kinetic energy to the potential energy density and defines atomic energies within each volume bounded by zero flux surface of the gradient of electron density. However, this results in charged units (so-called "Bader charges") that have long-range forces. Thus it is arbitrary to assign the energy to one region when it is in fact shared by interacting regions. Also, the Bader approach does not consider the exchange-correlation energy of DFT. A recent paper¹⁶ has reported a way to include such terms in a form of the virial theorem; they found values different from those given by the original method, making the applicability of a local virial theorem to DFT questionable. To overcome these difficulties, we instead define two integration volumes: one based on kinetic energy and the other based on potential (electrostatic) energy.

We derive the energy density methodology for PAW and apply it to several defect types in solid-state systems. Section II reviews the energy density expression derived by Chetty and Martin for NCPPs and derives the reformulated expression for the PAW method. The energy density contains a gauge-dependent kinetic energy density, a gauge-dependent long-range classical Coulomb energy density, a well-defined exchange-correlation energy density, and short-range terms grouped in an on-site energy for each ion. We also consider the method for integrating gauge-dependent terms. Section III presents four applications: the (110) surface energy of GaAs, the monovacancy formation energy of Si, the convergence test of (100) surface energy of Au, and the interstitial formation energy of O in a hexagonal close-packed Ti crystal. These examples show the generality of the method and the new information extracted such as the convergence of formation energy with size and the spatial partitioning of defect energy.

II. METHODOLOGY

In DFT, the standard form for the total energy of a crystal is usually written in reciprocal space. There are many forms convenient for the total energy written in terms of the wave functions and/or eigenvalues.¹⁷ For our purposes, we consider the expressions in real space, where the Kohn-Sham wave functions are used only for the kinetic energy and for nonlocal terms in the pseudopotential. In the NCPP approximation, the total energy is, in atomic units ($\hbar = m_e = e = 4\pi/\epsilon_0 = 1$),

$$\begin{aligned}
E_{\text{tot}} = & -\frac{1}{2} \sum_{n\mathbf{k}} f_{n\mathbf{k}} \int d\mathbf{r} \tilde{\psi}_{n\mathbf{k}}^*(\mathbf{r}) \nabla^2 \tilde{\psi}_{n\mathbf{k}}(\mathbf{r}) + E_{\text{xc}}[\rho^e(\mathbf{r})] \\
& + \sum_{\mu} E_{\mu}^{\text{nl}} + \int d\mathbf{r} \rho^e(\mathbf{r}) \sum_{\mu} V_{\mu}^{\text{loc}}(\mathbf{r} - \mathbf{R}_{\mu}) \\
& + \frac{1}{2} \int d\mathbf{r} \rho^e(\mathbf{r}) V_{\text{H}}(\mathbf{r}) + \sum_{\mu < \nu} \frac{Z_{\mu} Z_{\nu}}{R_{\mu\nu}}, \quad (1)
\end{aligned}$$

where $\tilde{\psi}_{n\mathbf{k}}(\mathbf{r})$ and $f_{n\mathbf{k}}$ are the valence pseudo-wave function and the electron occupation number for the n^{th} band, for wave vectors \mathbf{k} within the first Brillouin zone and with valence electron density $\rho^e(\mathbf{r})$. The first term is the independent electron kinetic energy. The second is the exchange-correlation energy $E_{\text{xc}}[\rho^e(\mathbf{r})] = \int d\mathbf{r} \rho^e(\mathbf{r}) \varepsilon_{\text{xc}}(\rho^e(\mathbf{r}), |\nabla(\rho^e(\mathbf{r}))|)$, where ε_{xc} is the exchange-correlation energy per electron; in the LDA or a generalized gradient^{18–20} approximation (GGA), it is a function of the density or the density and its gradient. The fermion nature of many-body interacting electrons is approximated by this exchange-correlation potential. The third term is the energy due to the nonlocal part of the pseudopotential

$$E_{\mu}^{\text{nl}} = \sum_{n\mathbf{k}} \sum_{\ell} \int d\mathbf{r} \tilde{\psi}_{n\mathbf{k}}^*(\mathbf{r}) V_{\mu\ell}^{\text{nl}}(|\mathbf{r} - \mathbf{R}_{\mu}|) \wp_{\ell} \tilde{\psi}_{n\mathbf{k}}(\mathbf{r}), \quad (2)$$

where $V_{\mu\ell}^{\text{nl}}$ is the ℓ th component of the nonlocal pseudopotential, with \wp_{ℓ} the projection operator on angular momentum ℓ . This term is site-localized (nonzero only within the core radius around a site), so that the total energy involves a sum over the sites μ at position \mathbf{R}_{μ} . The last three terms in Eq. (1) are the long-range Coulomb interactions. The fourth and fifth terms are the interaction of the electrons with the local ionic pseudopotential $V_{\mu}^{\text{loc}}(\mathbf{r} - \mathbf{R}_{\mu})$ and with themselves, which can be written as one-half the interaction with the Hartree potential $V_{\text{H}}(\mathbf{r}) = \int d\mathbf{r}' \frac{\rho^e(\mathbf{r}')}{|\mathbf{r} - \mathbf{r}'|}$. The sixth term is the valence charge Z_{μ} of ion μ at position \mathbf{R}_{μ} —the ion-ion Coulomb interaction energy, which is the same as for point charges since the cores are assumed not to overlap. Finally, there can be nonlinear core corrections, not shown here, which can be expressed in terms of E_{xc} involving a core density similar to the PAW method.

We use the PAW method¹¹ for calculations, where the total energy has a similar form:

$$\begin{aligned}
E_{\text{tot}} = & -\frac{1}{2} \sum_{n\mathbf{k}} f_{n\mathbf{k}} \int d\mathbf{r} \tilde{\psi}_{n\mathbf{k}}^*(\mathbf{r}) \nabla^2 \tilde{\psi}_{n\mathbf{k}}(\mathbf{r}) + E_{\text{xc}}[\tilde{\rho} + \hat{\rho} + \tilde{\rho}_c] \\
& + \sum_{\mu} (E_{\mu}^1 - \tilde{E}_{\mu}^1) + E_{\text{H}}[\tilde{\rho} + \hat{\rho}] \\
& + \int V_{\text{H}}[\tilde{\rho}_{Zc}](\tilde{\rho} + \hat{\rho}) d\mathbf{r} + \sum_{\mu < \nu} \frac{Z_{\mu} Z_{\nu}}{R_{\mu\nu}}, \quad (3)
\end{aligned}$$

$$\begin{aligned}
E_{\mu}^1 = & \sum_{ij} \rho_{ij} \langle \phi_i | -\frac{1}{2} \nabla^2 | \phi_j \rangle + \overline{E_{\text{xc}}[\rho^1 + \rho_c]} + \overline{E_{\text{H}}[\rho^1]} \\
& + \int V_{\text{H}}[\rho_{Zc}](\rho^1) d\mathbf{r}, \quad (4) \\
\tilde{E}_{\mu}^1 = & \sum_{ij} \rho_{ij} \langle \tilde{\phi}_i | -\frac{1}{2} \nabla^2 | \tilde{\phi}_j \rangle + \overline{E_{\text{xc}}[\tilde{\rho}^1 + \hat{\rho} + \tilde{\rho}_c]} \\
& + \overline{E_{\text{H}}[\tilde{\rho}^1 + \hat{\rho}]} + \int V_{\text{H}}[\tilde{\rho}_{Zc}](\tilde{\rho}^1 + \hat{\rho}) d\mathbf{r},
\end{aligned}$$

for $i, j = l m \varepsilon$. Quantities with a tilde are obtained by pseudization, and a superscript 1 indicates quantities evaluated inside atom-centered spheres on a radial grid. For each atom-centered sphere, the pseudopartial waves $|\tilde{\phi}_i\rangle$ match all-electron partial waves $|\phi_i\rangle$ at the sphere boundary and outside the augmentation region. The smooth projector functions $|\tilde{p}_i\rangle$ are dual to the

pseudopartial waves, and $\rho_{ij} = \sum_{n\mathbf{k}} f_{n\mathbf{k}} \langle \tilde{\psi}_{n\mathbf{k}} | \tilde{p}_i \rangle \langle \tilde{p}_j | \tilde{\psi}_{n\mathbf{k}} \rangle$ are the occupancies of augmentation orbitals (i, j). Then $\tilde{\rho}$ is the soft pseudovalence electron density, ρ^1 and $\tilde{\rho}^1$ are the on-site charges (full and pseudized) localized around each atom, $\hat{\rho}$ is the compensation charge, ρ_c and $\tilde{\rho}_c$ are the frozen core charges (full and pseudized), and ρ_{Zc} and $\tilde{\rho}_{Zc}$ are the sum of the nuclei ρ_Z and core charges (full and pseudized). The electrostatic interactions—electron-electron, electron-ion, and ion-ion interactions [last three terms in Eq. (3)]—are collectively the “classical Coulomb” energy. The short-range terms for individual ions are $E_{\text{on-site}} = (E_\mu^1 - \tilde{E}_\mu^1)$. We derive the total energy density for the PAW and pseudopotential methods as

$$e(\mathbf{r}) = t(\mathbf{r}) + e_{\text{cc}}(\mathbf{r}) + e_{\text{xc}}(\mathbf{r}) + E_{\text{on-site}} \delta(\mathbf{r} - \mathbf{R}_\mu) \quad (5)$$

and use gauge-independent integration over Bader and charge-neutral volumes to define atom-centered energies.

A. Kinetic energy density

The kinetic energy density is gauge dependent and can be expressed as an asymmetric or a symmetric functional:¹⁷

$$t^{(a)}(\mathbf{r}) = -\frac{1}{2} \sum_{n\mathbf{k}} f_{n\mathbf{k}} \tilde{\psi}_{n\mathbf{k}}^*(\mathbf{r}) \nabla^2 \tilde{\psi}_{n\mathbf{k}}(\mathbf{r}), \quad (6)$$

$$t^{(s)}(\mathbf{r}) = \frac{1}{2} \sum_{n\mathbf{k}} f_{n\mathbf{k}} |\nabla \tilde{\psi}_{n\mathbf{k}}(\mathbf{r})|^2.$$

The difference between the asymmetric and the symmetric kinetic energy density is a gauge-dependent term proportional to the Laplacian of pseudo electron density,

$$t^{(a)}(\mathbf{r}) - t^{(s)}(\mathbf{r}) = -\frac{1}{4} \nabla^2 \tilde{\rho}(\mathbf{r}). \quad (7)$$

The integral of the two forms of kinetic energy density is equal when the gauge-dependent integral vanishes, for example, for infinite or periodic systems. In Sec. II E, we integrate over a discrete set of atom-centered volumes where the gauge-dependent integrals also vanish—hence, uniquely defined kinetic energies for atoms in a condensed system. Note that continuous wave functions can have cusps in their gradients, thus the asymmetric form of the kinetic energy density can be ill-defined. Chetty and Martin chose the symmetric form for the kinetic energy density as it appears in the variational derivation of the Schrödinger’s equation,²¹ and hence it is a more fundamental quantity. However, the kinetic energy density is unique except for terms proportional to the Laplacian of pseudo-electron density; if we integrate over volumes such that the gauge-dependent term of Eq. (7) is zero (cf. Sec. II E), then either form of Eq. (6) gives the same kinetic energy. For a plane-wave basis, the *asymmetric* kinetic energy density is well-defined everywhere—that is, there are no cusps in the wave-function gradient—and is computationally less demanding to calculate. In the PAW method, the total kinetic energy density contains three terms:

$$t^{(a)}(\mathbf{r}) = \tilde{t}^{(a)}(\mathbf{r}) + t^{1(a)}(\mathbf{r}) - \tilde{t}^{1(a)}(\mathbf{r}). \quad (8)$$

The first term, $\tilde{t}^{(a)}(\mathbf{r})$, is also the first term in Eq. (3) and is expressed by using the pseudo-wave function. The on-site kinetic energies $t^{1(a)}(\mathbf{r})$ and $\tilde{t}^{1(a)}(\mathbf{r})$ are the first terms in

Eq. (4) and are included in the short-range on-site energy $E_{\text{on-site}} \delta(\mathbf{r} - \mathbf{R}_\mu)$.

B. Classical Coulomb energy density

The total classical Coulomb energy of a system with electrons and nuclei can be written as

$$E_{\text{cc}} = \frac{1}{2} \int d\mathbf{r} \int d\mathbf{r}' \frac{\rho^e(\mathbf{r}) \rho^e(\mathbf{r}')}{|\mathbf{r} - \mathbf{r}'|} + \int d\mathbf{r} \rho^e(\mathbf{r}) \sum_{\mu} V_{\mu}^{\text{loc}}(\mathbf{r}) + \sum_{\mu < \nu} \frac{Z_{\mu} Z_{\nu}}{R_{\mu\nu}}, \quad (9)$$

where $\rho^e(\mathbf{r})$ represents the pseudo-electron density in NCPPs, and the sum of pseudo-electron density $\tilde{\rho}(\mathbf{r})$ and compensation charge $\hat{\rho}(\mathbf{r})$ for the USPPs and the PAW method, μ and ν represent different nuclei, and $R_{\mu\nu}$ is the distance between two nuclei. There are various ways to calculate the electrostatic energy.¹⁷ In the Ewald method,⁶ terms are grouped with a Gaussian charge density around each atom so that the sum can be calculated by sums in both real and reciprocal space. However, this is not useful for constructing an energy density in real space. Instead, methods that involve only smooth densities for each ion can be used to construct expressions for the Coulomb energy that are expressed only in real space.

1. Smeared ions

We introduce a fictitious localized charge distribution ρ_{μ}^{loc} , which gives rise to a local pseudopotential V_{μ}^{loc} (cf. Sec. F.3 in Ref. 17) for ion μ as

$$\rho_{\mu}^{\text{loc}}(\mathbf{r} - \mathbf{R}_{\mu}) = -\frac{1}{4\pi} \nabla^2 V_{\mu}^{\text{loc}}(\mathbf{r} - \mathbf{R}_{\mu}). \quad (10)$$

The Coulomb interaction energy between two ions μ and ν is

$$E_{\mu\nu}^{\text{loc}}(|\mathbf{R}_{\mu\nu}|) = \frac{Z_{\mu} Z_{\nu}}{R_{\mu\nu}} = \int d\mathbf{r} \rho_{\mu}^{\text{loc}}(\mathbf{r} - \mathbf{R}_{\mu}) V_{\nu}^{\text{loc}}(\mathbf{r} - \mathbf{R}_{\nu}), \quad (11)$$

and the self-energy on each ion is

$$E_{\mu}^{\text{self}} = \frac{1}{2} \int d\mathbf{r} \rho_{\mu}^{\text{loc}}(\mathbf{r}) V_{\mu}^{\text{loc}}(\mathbf{r}). \quad (12)$$

The total classical Coulomb energy of a system with electrons and nuclei can be written as

$$E_{\text{cc}} = \frac{1}{2} \int d\mathbf{r} \int d\mathbf{r}' \frac{\rho^e(\mathbf{r}) \rho^e(\mathbf{r}')}{|\mathbf{r} - \mathbf{r}'|} + \int d\mathbf{r} \rho^e(\mathbf{r}) \sum_{\mu} V_{\mu}^{\text{loc}}(\mathbf{r}) + \sum_{\mu < \nu} \frac{Z_{\mu} Z_{\nu}}{R_{\mu\nu}} = \int d\mathbf{r} \frac{1}{8\pi} |\nabla V^{\text{tot}}(\mathbf{r})|^2 - \sum_{\mu} E_{\mu}^{\text{self}}, \quad (13)$$

with total classical Coulomb potential $V^{\text{tot}}(\mathbf{r}) = V_{\text{H}}(\mathbf{r}) + V^{\text{loc}}(\mathbf{r})$. The Hartree, local, and ion-ion interaction terms [last three terms in Eq. (3)] are combined into the classical Coulomb term.

We use the Maxwell energy for the total electrostatic component of the energy density. As a fictitious charge density defined in Eq. (10), the total neutral charge density is $\rho^{\text{tot}}(\mathbf{r}) = \rho^e(\mathbf{r}) + \rho^{\text{loc}}(\mathbf{r})$. With this definition, the Maxwell

form of the classical Coulomb energy density can be written as

$$e_{\text{cc}}^{\text{Maxwell}}(\mathbf{r}) = \frac{1}{8\pi} |\nabla V^{\text{tot}}(\mathbf{r})|^2. \quad (14)$$

Similar to the kinetic energy density, the classical Coulomb energy density is unique up to a gauge transformation. The asymmetric form of the classical Coulomb energy density is

$$e_{\text{cc}}^{(a)}(\mathbf{r}) = -\frac{1}{8\pi} V^{\text{tot}}(\mathbf{r}) \nabla^2 V^{\text{tot}}(\mathbf{r}) = \frac{1}{2} V^{\text{tot}}(\mathbf{r}) \rho^{\text{tot}}(\mathbf{r}), \quad (15)$$

and the gauge-dependent term is the difference between Eqs. (14) and (15),

$$e_{\text{cc}}^{(a)}(\mathbf{r}) - e_{\text{cc}}^{\text{Maxwell}}(\mathbf{r}) = -\frac{1}{8\pi} \nabla \cdot [V^{\text{tot}}(\mathbf{r}) \nabla V^{\text{tot}}(\mathbf{r})]. \quad (16)$$

As with the kinetic energy density, we can obtain a gauge-independent classical Coulomb energy as an integral over any volume bounded by a zero-flux surface of the gradient of the total Coulomb potential.

The PAW method introduces the soft compensation-charge \tilde{n} , and the Hartree energy is

$$\begin{aligned} E_{\text{H}} &= \tilde{E}_{\text{H}} + (E_{\text{H}}^1 - \tilde{E}_{\text{H}}^1) \\ &= E_{\text{H}}[\tilde{\rho} + \hat{\rho}] + \sum_{\mu} \overline{E_{\text{H}}[\rho^1]} - \sum_{\mu} \overline{E_{\text{H}}[\hat{\rho}^1 + \hat{\rho}]}. \end{aligned} \quad (17)$$

The first term is related to the soft valence-charge density and the soft compensation-charge density, and is included in the classical Coulomb energy density. The last two short-range terms are related to the short-range on-site energy $E_{\text{on-site}} \delta(\mathbf{r} - \mathbf{R}_{\mu})$, as are the electron-ion interactions.

2. Model charge density

In practice, the local charge density due to local pseudopotential can vary rapidly (cf. Fig. 1), which causes numerical errors in a real calculation. To improve our numerical accuracy, we then introduce a model charge density $\rho^{\text{model}}(\mathbf{r})$ to solve this problem. The model charge density is chosen as obeying following constraints: a spherically symmetric functional, which is centered at each ion, 0 beyond the cutoff radius of the local pseudopotential, and normalized as negative of the local charge density within the cutoff radius. The total charge density can be rewritten as

$$\begin{aligned} \rho^{\text{tot}}(\mathbf{r}) &= \rho^{\text{loc}}(\mathbf{r}) + \rho^{\text{model}}(\mathbf{r}) + \rho^e(\mathbf{r}) - \rho^{\text{model}}(\mathbf{r}) \\ &= \sum_{\mu} [\rho_{\mu}^{\text{loc}}(\mathbf{r}) + \rho_{\mu}^{\text{model}}(\mathbf{r})] + \delta\rho(\mathbf{r}), \end{aligned} \quad (18)$$

where $\rho_{\mu}^{\text{loc}}(\mathbf{r}) + \rho_{\mu}^{\text{model}}(\mathbf{r})$ is a neutral and spherical charge density for each ion; $\delta\rho(\mathbf{r})$ is the difference between the valence electronic charge density and the model charge density. The asymmetric form of the classical Coulomb energy is

$$\begin{aligned} E_{\text{cc}}[\rho^{\text{tot}}] &= E_{\text{cc}}[\rho^{\text{loc}} + \rho^{\text{model}}] + \int d\mathbf{r} (V^{\text{loc}} + V^{\text{model}}) \delta\rho \\ &\quad + \frac{1}{2} \int d\mathbf{r} \delta V_{\text{H}}[\delta\rho] \delta\rho - \sum_{\mu} E_{\mu}^{\text{self}}. \end{aligned} \quad (19)$$

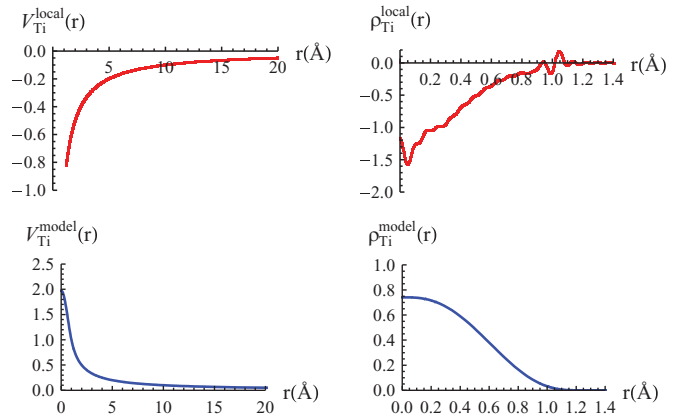


FIG. 1. (Color online) Local pseudopotential and charge density for PAW Ti (top) and compensating model potential and charge density (bottom). The PAW-GGA potential for Ti has a cutoff radius of 1.22 Å; the charge density—given by the Laplacian of the potential—can have short-wavelength oscillations that are well represented on a radial grid but poorly represented on a regular Cartesian grid. To compensate for this, we add a smooth model potential and corresponding charge density that matches outside of the cutoff radius. The model potential $V^{\text{model}}(\mathbf{r})$ is a smoothly varying long-range potential; the model charge density $\rho^{\text{model}}(\mathbf{r})$ is also a smoothly varying function for the radius r from 0 to the cutoff radius r_c , which integrates to the negative charge density of the local charge.

The first term is

$$E_{\text{cc}}[\rho^{\text{loc}} + \rho^{\text{model}}] = \sum_{\mu < \nu} E_{\mu\nu}^{\text{loc+model}}(|\mathbf{R}_{\mu\nu}|) + \sum_{\mu} E_{\mu}^{\text{loc+model}}. \quad (20)$$

The electronic interaction between two neutral atoms is 0 when there is no charge overlap, since all moments are 0 for spherical charge distributions. Therefore, the first term in Eq. (20) is 0. Combining the second term with the self-energy in Eq. (12), we have

$$\begin{aligned} E_{\mu}^{\text{loc+model}} - E_{\mu}^{\text{self}} &= \frac{1}{2} \int d\mathbf{r} V_{\mu}^{\text{model}}(\mathbf{r}) \rho_{\mu}^{\text{model}}(\mathbf{r}) \\ &\quad + \int d\mathbf{r} V_{\mu}^{\text{loc}}(\mathbf{r}) \rho_{\mu}^{\text{model}}(\mathbf{r}), \end{aligned} \quad (21)$$

which is a constant for each species of ions and can be canceled when studying the defect energies. Neglecting this constant term, the asymmetric form of the classical Coulomb energy density in Eq. (19) is

$$\begin{aligned} e_{\text{cc}}(\mathbf{r}) &= [V^{\text{loc}}(\mathbf{r}) + \frac{1}{2} V_{\text{H}}(\mathbf{r}) \\ &\quad + \frac{1}{2} V^{\text{model}}(\mathbf{r})] [\rho^e(\mathbf{r}) - \rho^{\text{model}}(\mathbf{r})], \end{aligned} \quad (22)$$

where $V^{\text{loc}}(\mathbf{r})$, $V_{\text{H}}(\mathbf{r})$, and $\rho^e(\mathbf{r})$ are already known in real space. Different model potential $V^{\text{model}}(\mathbf{r})$ and model charge density $\rho^{\text{model}}(\mathbf{r})$ can be constructed as long as they obey above constraints. In this work, the model charge density is a polynomial functional with continuous zeroth-, first- and second-order derivatives at 0 and r_c ; for $u = r/r_c$,

$$\rho_{\mu}^{\text{model}}(r) = \begin{cases} \frac{21}{5\pi r_c^3} [1 - 10u^3 + 15u^4 - 6u^5], & r < r_c, \\ 0, & r > r_c. \end{cases} \quad (23)$$

As shown in Fig. 1 the local charge density varies rapidly with respect to radius r , while the model charge density parametrized in Eq. (23) smoothly decays to 0 with increasing r to r_c . The corresponding potential is

$$V_\mu^{\text{model}}(r) = \begin{cases} \frac{1}{5r_c} [12 - 14u^2 + 28u^5 - 30u^6 + 9u^7], & r < r_c, \\ 1/r, & r > r_c. \end{cases} \quad (24)$$

The model charge density gives faster numerical convergence on a regular spatial grid compared to the rapidly varying local charge density. This model charge density has been tested by calculating the surface energy based on a Si bulk (8 atom) and a Si (111) slab (16 atom). The energy difference between the values calculated by total energy calculation and those calculated by energy density integration is about 7 meV. It has also been tested on O atoms and on O₂ molecules for various grid sizes, where we had a convergence problem upon using a rapidly varying local charge density. For a wide range of grid sizes, the total energy calculations converge to a precision of 1 meV, while the difference between results calculated by these two methods is up to 0.4 eV. However, the energy difference can be reduced below 1 meV with the smooth model charge.

C. Exchange-correlation energy density

The exchange-correlation energy of many-body interacting electrons can be expressed in terms of an exchange-correlation hole that tends to be localized around each electron. In DFT it is usually treated as a function of the local density and its gradients, which is determined by the choice of exchange-correlation functional. For both the LDA and the GGA, the gauge-independent exchange-correlation energy density is

$$e_{\text{xc}}(\mathbf{r}) = \rho^e(\mathbf{r}) \varepsilon_{\text{xc}}[\rho^e(\mathbf{r}), |\nabla \rho^e(\mathbf{r})|], \quad (25)$$

where ε_{xc} is the exchange-correlation energy per electron.

D. On-site energy

The last term of the energy density in Eq. (5) is short-ranged. For the PAW method, the on-site energy for each ion is composed of the kinetic energy, exchange-correlation energy, and Coulomb energy, including electron-electron and electron-ion interactions in the augmentation region, and is

$$E_{\text{on-site}} = (E_\mu^1 - \tilde{E}_\mu^1) \delta(\mathbf{r} - \mathbf{R}_\mu), \quad (26)$$

with the on-site energies E_μ^1 and \tilde{E}_μ^1 expressed in Eq. (4). In practice, we calculate E_μ^1 and \tilde{E}_μ^1 for each ion using radial grids. For NCPPs and USPPs, this short-range term corresponds to the nonlocal pseudopotential energy. For USPPs,

$$E_\mu^{\text{nl}} = \sum_{n\mathbf{k}} \int d\mathbf{r} \tilde{\psi}_{n\mathbf{k}}^*(\mathbf{r}) \left(\sum_{ij} D_{ij}^{\text{ion}} |\beta_i\rangle \langle \beta_j| \right) \tilde{\psi}_{n\mathbf{k}}(\mathbf{r}), \quad (27)$$

where the coefficients D_{ij}^{ion} and the projector functions $|\beta_i\rangle$ vary depending on the atomic species. For NCPPs,

$$E_\mu^{\text{nl}} = \sum_{n\mathbf{k}} \sum_{\ell} \int d\mathbf{r} \tilde{\psi}_{n\mathbf{k}}^*(\mathbf{r}) V_{\mu\ell}^{\text{nl}}(|\mathbf{r} - \mathbf{R}_\mu|) \wp_{\ell} \tilde{\psi}_{n\mathbf{k}}(\mathbf{r}). \quad (28)$$

E. Gauge dependence and uniqueness

We have two energy density terms to be integrated that are gauge dependent: the kinetic energy density and the classic Coulomb energy density. Defining a gauge-independent energy requires integrating these energy densities over volumes to cancel out any gauge dependence. Previously, Chetty and Martin² integrated over Wigner-Seitz cells in a supercell; Rapcewicz *et al.*⁹ constructed a Voronoi polyhedron for each comprised atom. However, these volumes are not the *general* solution to removing gauge dependence. For the kinetic energy density, the gauge dependence, Eq. (7), is proportional to the Laplacian of electronic charge density. Hence, we integrate over a volume where the gradients of electron density has a zero component along the surface normal direction \hat{n} , $\nabla \rho(\mathbf{r}) \cdot \hat{n} = 0$: the zero-flux ‘‘Bader’’ volume.¹⁵ For the classical Coulomb energy density, the gauge dependence, Eq. (16), is proportional to the Laplacian of the potential. Hence, we integrate over a volume where the electrostatic field has a zero component along the surface normal direction \hat{n} , $\nabla V(\mathbf{r}) \cdot \hat{n} = 0$: the zero-flux charge-neutral volume.

In this work, we construct two volumes: the Bader volume is used to integrate kinetic energy density and exchange-correlation energy density, and the charge-neutral volume is used to integrate classical Coulomb energy density. Each of these volumes is ‘‘atom centered’’—that is, it contains one atom somewhere in the volume—and they each partition space: the union of all volumes is the total supercell volume, and the intersection of any two volumes is 0. We define these volumes on the same regular spatial grid used to represent the charge density and energy density terms. Accurate definition of the volumes and integration uses a weighted integration scheme²² that has quadratic convergence in the grid density. Finally, we use the integral over the gauge-dependent kinetic [Eq. (7)] and classical Coulomb [Eq. (16)] terms as an estimate of the integration error for atomic energies. This error estimate has a sign, so it is possible for the magnitude of the error of the energies of neighboring volumes A and B to be *greater* than the magnitude of error integrating over $A \cup B$.

F. Summary

We summarize the procedure for calculating atomic energy using the energy density method in Table I. The total energy density in Eq. (5) contains a gauge-dependent kinetic energy density, a gauge-dependent classical Coulomb energy density, a gauge-independent exchange-correlation energy density, and a short-range on-site energy. The well-defined atomic energy can be calculated with two different integration volumes. The Bader volume is employed for the integral of the kinetic energy and the exchange-correlation energy, and the charge neutral volume for the integral of the classical Coulomb energy.

III. APPLICATIONS

To verify our implementation of the energy density method and highlight the new information it reveals, we perform DFT calculations with VASP on the GaAs(110) surface, Si monovacancy, Au(100) surface, and O interstitial in Ti. We integrate the energy densities around the defect regions and compare the integrated defect energies with values given

TABLE I. Summary of the energy density formulas for the PAW, USPP, and NCPP methods and the procedure for calculating atomic energy using the energy density method.

$e(\mathbf{r}) = t(\mathbf{r}) + e_{cc}(\mathbf{r}) + e_{xc}(\mathbf{r}) + E_{\text{on-site}}\delta(\mathbf{r} - \mathbf{R}_\mu).$	(5)
(1) Kinetic energy density	
$t^{(s)}(\mathbf{r}) = \frac{1}{2} \sum_{n\mathbf{k}} f_{n\mathbf{k}} \nabla \tilde{\psi}_{n\mathbf{k}}(\mathbf{r}) ^2.$	
$t^{(a)}(\mathbf{r}) = -\frac{1}{2} \sum_{n\mathbf{k}} f_{n\mathbf{k}} \tilde{\psi}_{n\mathbf{k}}^*(\mathbf{r}) \nabla^2 \tilde{\psi}_{n\mathbf{k}}(\mathbf{r}).$	(6)
$t^{(a)}(\mathbf{r}) - t^{(s)}(\mathbf{r}) = -\frac{1}{4} \nabla^2 \tilde{\rho}(\mathbf{r}).$	(7)
Construct zero-flux volume Ω_ρ , where $\nabla \tilde{\rho}(\mathbf{r}) \cdot \hat{n} = 0.$	
Bounded volume integral, $T = \int_{\Omega_\rho} t(\mathbf{r}).$	
(2) Classical Coulomb energy density	
$e_{cc}^{\text{Maxwell}}(\mathbf{r}) = \frac{1}{8\pi} \nabla V^{\text{tot}}(\mathbf{r}) ^2.$	(14)
$e_{cc}^{(a)}(\mathbf{r}) = \frac{1}{2} V^{\text{tot}}(\mathbf{r}) \rho^{\text{tot}}(\mathbf{r})$	(15)
$= [V^{\text{loc}}(\mathbf{r}) + \frac{1}{2} V_{\text{H}}(\mathbf{r}) + \frac{1}{2} V^{\text{model}}(\mathbf{r})][\rho^e(\mathbf{r}) - \rho^{\text{model}}(\mathbf{r}).]$	(22)
$e_{cc}^{(a)}(\mathbf{r}) - e_{cc}^{\text{Maxwell}}(\mathbf{r}) = -\frac{1}{8\pi} \nabla \cdot [V^{\text{tot}}(\mathbf{r}) \nabla V^{\text{tot}}(\mathbf{r}).]$	(16)
Construct zero-flux volume Ω_V , where $\nabla V^{\text{tot}}(\mathbf{r}) \cdot \hat{n} = 0.$	
Bounded volume integral, $E_{cc} = \int_{\Omega_V} e_{cc}(\mathbf{r}).$	
(3) Exchange-correlation energy density	
$e_{xc}(\mathbf{r}) = \rho^e(\mathbf{r}) \varepsilon_{xc}[\rho^e(\mathbf{r}), \nabla \rho^e(\mathbf{r})].$	(25)
Bounded volume integral, $E_{xc} = \int_{\Omega_\rho} e_{xc}(\mathbf{r}).$	
(4) On-site energies	
PAW: $E_{\text{on-site}} = (E_\mu^1 - \tilde{E}_\mu^1).$	(26)
USPPs: $E_\mu^{\text{nl}} = \sum_{n\mathbf{k}} \int d\mathbf{r} \tilde{\psi}_{n\mathbf{k}}^*(\mathbf{r}) \left(\sum_{ij} D_{ij}^{\text{ion}} \beta_i\rangle \langle \beta_j \right) \tilde{\psi}_{n\mathbf{k}}(\mathbf{r}).$	(27)
NCPPs: $E_\mu^{\text{nl}} = \sum_{n\mathbf{k}} \sum_\ell \int d\mathbf{r} \tilde{\psi}_{n\mathbf{k}}^*(\mathbf{r}) V_{\mu\ell}^{\text{nl}}(\mathbf{r} - \mathbf{R}_\mu) \delta_{\ell} \tilde{\psi}_{n\mathbf{k}}(\mathbf{r}).$	(28)
Atomic energy: $E = T + E_{cc} + E_{xc} + E_{\text{on-site}}.$	

by total energy calculations and experiments. Finally, the convergence of the atomic energy to bulk values within a *single* calculation shows the convergence (or lack of it) for each calculation.

A. GaAs(110) surface

The GaAs(110) surface contains equal numbers of Ga and As atoms: a stoichiometric or nonpolar surface. The surface energy γ_{surf} of a stoichiometric slab is

$$\gamma_{\text{surf}} = \frac{1}{2A} \left(E_{\text{slab}} - N_{\text{slab}} \frac{E_{\text{bulk}}}{N_{\text{bulk}}} \right), \quad (29)$$

for surface area A , where E_{slab} is the total energy of a GaAs slab with N_{slab} pairs of GaAs atoms, and E_{bulk} is the total energy of GaAs bulk with N_{bulk} pairs of atoms. Our DFT calculations are performed with the PAW method,¹¹ with the LDA^{4,5} for the exchange-correlation energy. The valence configurations for Ga is $[\text{Ar}]3d^{10}4s^24p^1$ with cutoff radius 1.01 Å, and As is $([\text{Ar}]3d^{10})4s^24p^3$ with cutoff radius 1.11 Å; this requires a plane-wave basis set with a cutoff energy of 650 eV. This gives a lattice constant of 5.6138 Å for zincblende GaAs, compared with the experimental lattice constant of 5.65 Å. The supercell contains 11 layers of atoms, with a pair of GaAs atoms on each layer, and a vacuum gap of 8 Å to prevent interaction between slabs under periodic boundary conditions. We use Monkhorst-Pack k -point meshes²³ of $8 \times 8 \times 8$ for bulk eight-atom cells and $8 \times 8 \times 1$ for the slab supercell; Brillouin-zone

integration uses Gaussian smearing with $k_B T = 0.1$ eV for electronic occupancies, and the total energy extrapolated to $k_B T = 0$ eV. We represent the charge density and compute energy densities on a grid of $84 \times 120 \times 560$. Geometry is optimized to reduce forces below 5 meV/Å. This gives a surface energy of 50 meV/Å²; this agrees with Moll *et al.*'s value²⁴ of 52 meV/Å², Qian *et al.*'s value²⁵ of 57 meV/Å², Choudhury *et al.*'s²⁶ LDA value of 50 meV/Å², and the experimental value²⁷ of 54 ± 9 meV/Å².

Figure 2 shows the energy change from bulk for each layer by integrating over volumes that eliminate gauge dependence. The change in energy shows differences from bulk that are mainly confined to the first two layers: the bulk-like response of the interior layers—not just for the total energy, but also for the individual contributions to the energy. Determining the size convergence of a surface calculation with total energy alone requires computing surface energies for multiple sizes; in our case, the bulk-like behavior of our center layers indicates a small finite-size error *without* requiring multiple size calculations. We can integrate the surface energy by adding the energies from the first two layers; our surface energy is 51 ± 1 meV/Å², which agrees well with the total-energy calculation of surface energy. The error estimate is specifically for the integration error over the Bader and charge-neutral volumes. Note, also, that we can compute the energy of each surface independently; for surfaces with different chemistry, this allows for two surface energies to be calculated from a single supercell.

Figure 3 shows the Bader and charge-neutral volumes for Ga and As atoms in a $(\bar{1}10)$ plane of GaAs. The Ga and As atoms all lie in a plane, and the intersection of the surfaces show the difference between the two atom-centered volumes. The Bader volumes have zero flux of the gradients of charge density through their surfaces and are used to integrate a unique kinetic and exchange-correlation energy. The charge-neutral volumes have zero flux with the total electrostatic field and are used to integrate a unique classical Coulomb energy. These volumes are also different from the Voronoi volumes around each atom. The atomic volumes, like the individual components of energy, become bulk-like in the center of the slab. Atoms at the free surfaces have volumes that extend into the vacuum. Besides the different surfaces, the Bader volumes of As are larger than the As charge-neutral volumes.

B. Si monovacancy

The monovacancy in bulk Si is a simple point defect in a semiconductor, which has been studied theoretically and experimentally. From total energies, the formation energy of a vacancy ΔH_v is

$$\Delta H_v = E_v^{N-1} - \frac{N-1}{N} E^N, \quad (30)$$

where E_v^{N-1} and E^N are the total energy of the $N-1$ and N atom supercells with and without one vacancy. Wright²⁸ performed LDA⁵ and GGA-PBE (Perdew, Burke, and Ernzerhof)¹⁸ calculations in 215-, 511-, and 999-atom supercells, to get formation energies of 3.53, 3.49, and 3.47 eV with LDA and 3.66, 3.63, and 3.62 eV with GGA. Puska *et al.*²⁹ performed LDA calculations in 31-, 63-, 127-, and

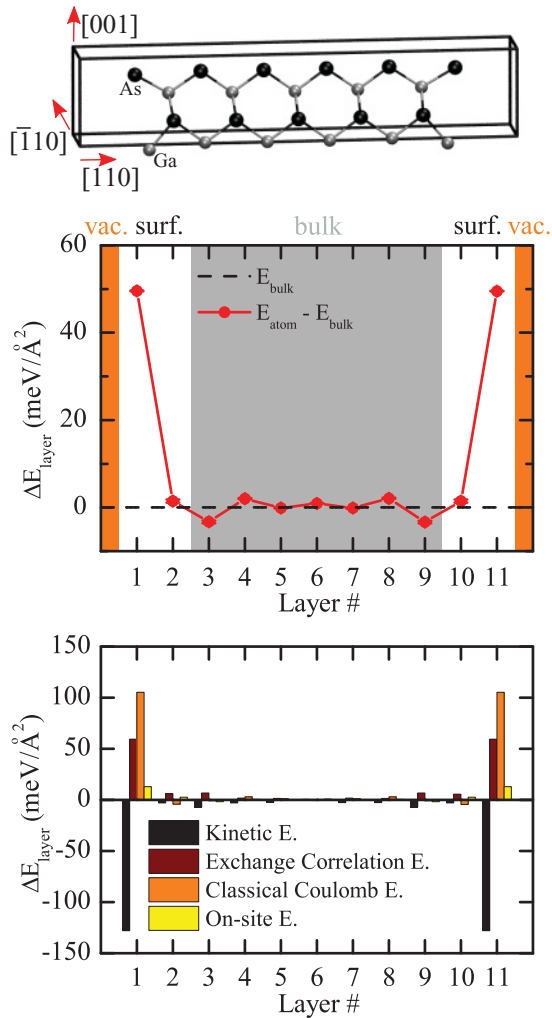


FIG. 2. (Color online) Atomic energy distribution on a GaAs(110) slab. The supercell contains 11 layers of GaAs. The energy density integrated over each atomic layer divided by the surface area gives the energy per layer referenced to the bulk value ΔE_{layer} . The atomic integration errors are smaller than $1 \text{ meV}/\text{\AA}^2$. The surface energy is confined to the first two layers. The bulk-like behavior of the center layers indicates sufficient thickness of the slab calculation. The individual energy term contribution to each layer is shown at the bottom. All energy terms are bulk-like for the center layers of the slab, not just the sum. At the surface, the kinetic energy decreases as the valence charge density spreads out into the vacuum.

215-atom supercells, to get formation energies of 3.98, 3.42, 3.44, and 3.31 eV. Experiments have found a formation energy of $3.6 \pm 0.2 \text{ eV}$.³⁰

Our DFT calculations are performed with the PAW method with the GGA of Perdew and Wang (PW91)¹⁹ for the exchange-correlation energy. The valence configuration for Si is $[\text{Ne}]3s^23p^2$, with cutoff radius 1.01 Å; this requires a plane-wave basis set with a cutoff energy of 417 eV. This gives a lattice constant of 5.4674 Å for diamond Si, compared with the experimental lattice constant of 5.43 Å. The $2 \times 2 \times 2$ simple cubic supercell with a vacancy contains 63 atoms. We use a $4 \times 4 \times 4$ Monkhorst-Pack k -point mesh; Brillouin-zone integration uses Gaussian smearing with $k_B T = 0.15 \text{ eV}$, and

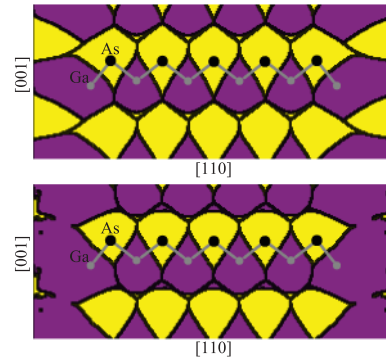


FIG. 3. (Color online) Top: Bader volumes and (bottom) charge-neutral volumes for Ga (purple/dark gray) and As (yellow/light gray) in a $(\bar{1}10)$ plane of GaAs. These integration volumes define the unique atomic kinetic and exchange-correlation energies and the classical Coulomb energies. Each volume contains a single atom, but the two volumes are different for the same atom.

the total energy extrapolated to $k_B T = 0 \text{ eV}$. We represent the charge density and compute energy densities on a grid of $200 \times 200 \times 200$. Geometry is optimized to reduce forces below $5 \text{ meV}/\text{\AA}$. This gives a formation energy of 3.65 eV.

Figure 4 shows the energy change from bulk for shells surrounding a Si vacancy. The primary contribution to the vacancy formation energy comes from the first five shells, which become bulk-like at larger distances. Summing the atomic energies up to the fifth shell gives a formation energy of $3.57 \pm 0.05 \text{ eV}$, which is similar to the total energy calculation. The importance of the fifth shell over the third and fourth shells can also be seen in the charge disturbances from a vacancy. Kane³¹ showed charge disturbances around a Si monovacancy out to the 27th shell, while the first two shells contribute 60% of the charge disturbance. The most striking feature was that charge concentrated on the $\{1\bar{1}0\}$ planar zigzag chains of atoms, such as $[000]$, $[111]$, $[220]$, $[331]$, and $[440]$. Twelve such chains exist by symmetry. After reaching the fifth shell at $\frac{a}{4}\langle 331 \rangle$, the charge decays monotonically along the coplanar chains. Kane connected this result to the importance of the fifth-neighbor interaction in the valence force model³² of covalent phonon spectra. The valence force model is an empirical model connecting force constants to the electronic configuration. The fifth-neighbor interaction is proportional to $r^2 \Delta\phi \Delta\phi'$ from changes in bond angles ϕ and ϕ' along a zigzag chain. The fifth neighbor has a stronger interaction with bond bending than the third and fourth neighbors; we see a similar change in energy for the vacancy.

C. Au(100) surface

Au(100) is a low-index metallic surface without a reconstruction. To calculate the surface energy with Eq. (29), the thickness of the slab must be increased until the surface energy γ_{surf} converges. Our DFT calculations are performed with the PAW method with the GGA of PBE¹⁸ for the exchange-correlation energy. The valence configuration for Au is $[\text{Xe}]6s^15d^{10}$, with cutoff radius 1.32 Å; this requires a plane-wave basis set with a cutoff energy of 400 eV. This

gives a lattice constant of 4.171 Å for FCC Au, compared with the experimental lattice constant of 4.08 Å. Supercells range from four through seven layers of atoms, with one Au atom on

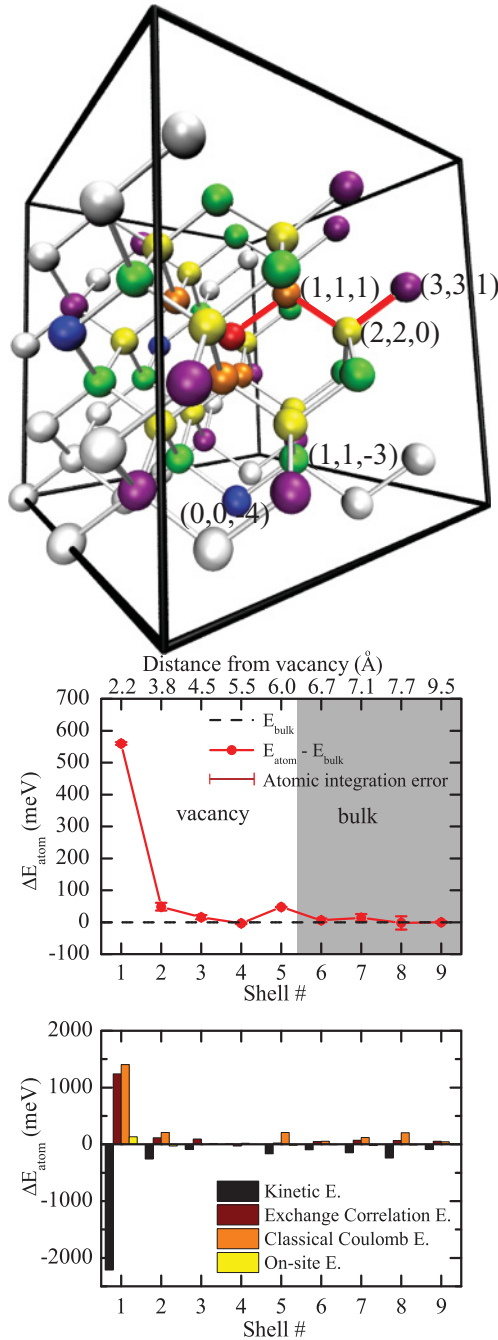


FIG. 4. (Color online) Si monovacancy in a $2 \times 2 \times 2$ simple cubic supercell with atomic energies. The first five shells are $\frac{a}{4}\langle 111 \rangle$ (orange/gray), $\frac{a}{4}\langle 220 \rangle$ (yellow/light gray), $\frac{a}{4}\langle 11\bar{3} \rangle$ (green/gray), $\frac{a}{4}\langle 004 \rangle$ (blue/dark gray), and $\frac{a}{4}\langle 331 \rangle$ (violet/dark gray). Only three shells have displacements greater than 0.01 Å: the first shell, with 4 atoms, relaxes inward by 0.17 Å; the second shell, with 12 atoms, relaxes inward by 0.05 Å; and the fifth shell relaxes inward by 0.02 Å. These three shells form a zigzag chain (red/gray) from the vacancy with a strong interaction. The atomic energy confirms this interaction, with energies of 560 ± 5 meV (first), 49 ± 12 meV (second), and 47 ± 1 meV (fifth), compared with 16 ± 7 meV (third) and -4 ± 3 meV (fourth). As with a free surface, the kinetic energy drops close to the vacancy due to decreasing valence charge density.

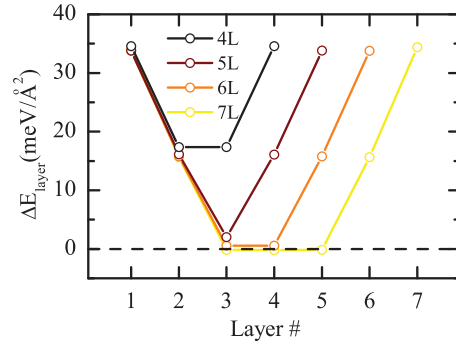


FIG. 5. (Color online) Atomic energy distribution on a Au(100) slab. Atomic integration errors are smaller than $1 \text{ meV}/\text{Å}^2$. The bulk-like behavior of the center layer(s) of five-, six-, and seven-layer slabs indicates sufficient thickness of the slab calculation.

each layer, and a vacuum gap of 10.5 Å to prevent interaction between slabs under periodic boundary conditions. We use Monkhorst-Pack k -point meshes of $13 \times 13 \times 13$ for bulk four-atom cells and $13 \times 13 \times 1$ for slab supercells; Brillouin-zone integration uses the Methfessel-Paxton method³³ with $k_B T = 0.2 \text{ eV}$ for electronic occupancies, and the total energy extrapolated to $k_B T = 0 \text{ eV}$. We represent the charge density and compute energy densities on a grid increasing from $60 \times 60 \times 350$ to $60 \times 60 \times 460$ for four- to seven-layer supercells. Geometry is optimized to reduce forces below $5 \text{ meV}/\text{Å}$. This gives surface energies of 53.3, 52.7, 52.5, and 52.3 $\text{meV}/\text{Å}^2$; these also agree with Zólyomi *et al.*'s value³⁴ of 54 $\text{meV}/\text{Å}^2$.

Figure 5 shows the energy change from bulk value for each layer of atoms. Energy density integration of the left (or right) two layers of four-layer slab gives a surface energy of $52 \pm 1 \text{ meV}/\text{Å}^2$; five-, six-, and seven-layer slabs all give a surface energy of $50 \pm 1 \text{ meV}/\text{Å}^2$. Although the calculated surface energy of a four-layer slab is close to the values for five-, six-, and seven-layer slab, the atomic energy distribution shows the center layers of the four-layer slab have not reached the bulk-like behavior. Unlike the convergence test of the traditional total energy calculation, the required thickness of a slab can be determined directly by observing the variation of atomic energy from the bulk value.

D. HCP Ti with interstitial O

Finally, we consider the formation energy of an interstitial oxygen in the octahedral site of HCP titanium. The formation energy is

$$E_I^{\text{Ti-O}} = E(\text{Ti} + \text{O}_i) - E(\text{Ti}) - \frac{1}{2}E(\text{O}_2), \quad (31)$$

where $E(\text{Ti} + \text{O}_i)$ and $E(\text{Ti})$ are the total energy of relaxed supercells with and without an oxygen atom, and $E(\text{O}_2)$ is the total energy of the oxygen molecule. Our DFT calculations are performed with the PAW method, with the GGA-PW91 for the exchange-correlation energy. The valence configuration for Ti is $[\text{Ne}]3s^2 3p^6 4s^2 3d^2$ with cutoff radius 1.22 Å, and O is $[\text{He}]2s^2 2p^4$ with cutoff radius 0.80 Å; this requires a plane-wave basis set with a cutoff energy of 500 eV. This gives lattice constants of $a = 2.933 \text{ Å}$, $c = 4.638 \text{ Å}$, and $c/a = 1.581$ for HCP Ti, compared with the experimental

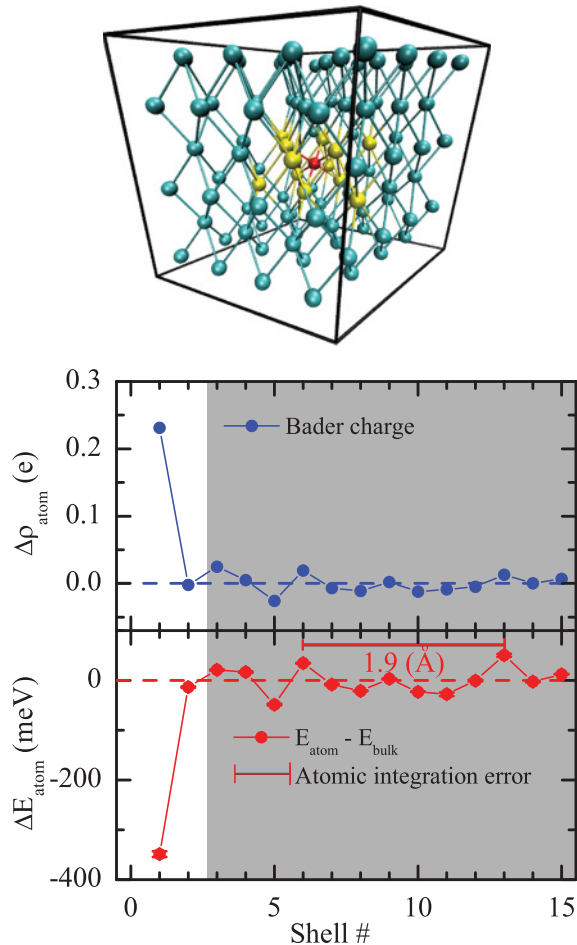


FIG. 6. (Color online) HCP Ti $4 \times 4 \times 3$ supercell with an interstitial O (red/gray) in an octahedral site. The formation energy is confined to the first two Ti shells (yellow/light gray); away from the oxygen atom, the charge density and energy density of Ti atoms experience Friedel-like oscillations. There is a charge transfer of $1.45e$ to the interstitial O atom.

lattice constants of $a = 2.951 \text{ \AA}$, $c = 4.684 \text{ \AA}$, and $c/a = 1.587$.³⁵ The supercell contains 96 Ti atoms ($4 \times 4 \times 3$) and 1 O atom. We use a $2 \times 2 \times 2$ Monkhorst-Pack k -point mesh; Brillouin-zone integration uses the Methfessel-Paxton method with $k_B T = 0.1 \text{ eV}$ for electronic occupancies, and the total energy extrapolated to $k_B T = 0 \text{ eV}$. We represent the charge density and compute energy densities on a grid of $180 \times 180 \times 216$. Geometry is optimized to reduce forces

below 20 meV/\AA . This gives an interstitial oxygen formation energy of -6.19 eV , with a nearest-neighbor distance between Ti and O of 2.08 \AA . Hennig *et al.*³⁶ performed GGA-PW91 calculations using ultrasoft Vanderbilt-type¹² pseudopotentials in the same supercell and found a formation energy of -6.12 eV and nearest-neighbor distances of 2.06 – 2.09 \AA .

Figure 6 shows the calculated Ti atomic energy change from the bulk value for each shell. The change in energy shows that the differences from bulk are mainly confined to the first two shells, with bulk-like behavior for shells farther away from the oxygen atom. The energy density and charge density oscillate and decay away from the interstitial. They peak at the 6th shell and the 13th shell with a wavelength of 1.9 \AA . Weiss's Compton profile³⁷ measured the Fermi momentum of Ti as $1.08 \pm 0.06 \text{ a.u.}$, which corresponds to a Friedel oscillation wavelength of 1.5 \AA . Jepson's³⁸ earlier calculation using the linear muffin-tin-orbital method obtained the Fermi energy of Ti as 0.667 Ryd , which corresponds to a Friedel oscillation wavelength of 2.0 \AA . Adding the atomic energy change of the first two shells from the interstitial O and the atomic energy change of the O atom, we obtain an interstitial formation energy of $-6.13 \pm 0.01 \text{ eV}$, which agrees with the total energy calculation.

IV. CONCLUSIONS

We implement the energy density method for PAW and USPPs for the plane-wave DFT code VASP and analyze surface energies from the energy density in the surface region and vacancy and interstitial formation energies from the energy density in the point defect region. The method can be applied to surfaces and defects in a variety of systems and produces defect formation energies comparable to well-converged total energy calculations. Furthermore, the energy density determines the distribution of energy near the defect or surface and the sufficiency of a supercell without a separate convergence test. It can also give separate defect formation energies from a single supercell calculation.

ACKNOWLEDGMENTS

This research was supported by the NSF under Grant No. DMR-1006077, and through the Materials Computation Center at UIUC (NSF Grant No. DMR-0325939), and with computational resources from NSF/TeraGrid provided by NCSA and TACC.

*Corresponding author: dtrinkle@illinois.edu

¹W. Kohn and L. J. Sham, *Phys. Rev. A* **140**, 1133 (1965).

²N. Chetty and R. M. Martin, *Phys. Rev. B* **45**, 6074 (1992).

³N. Troullier and J. L. Martins, *Phys. Rev. B* **43**, 1993 (1991).

⁴D. M. Ceperley and B. J. Alder, *Phys. Rev. Lett.* **45**, 566 (1980).

⁵J. P. Perdew and A. Zunger, *Phys. Rev. B* **23**, 5048 (1981).

⁶P. P. Ewald, *Ann. Phys.* **369**, 253 (1921).

⁷N. Chetty and R. M. Martin, *Phys. Rev. B* **45**, 6089 (1992).

⁸S. B. Zhang and S. H. Wei, *Phys. Rev. Lett.* **92**, 086102 (2004).

⁹K. Rapcewicz, B. Chen, B. Yakobson, and J. Bernholc, *Phys. Rev. B* **57**, 7281 (1998).

¹⁰R. Ramprasad, *J. Phys. Condens. Matter* **14**, 5497 (2002).

¹¹P. E. Blöchl, *Phys. Rev. B* **50**, 17953 (1994).

¹²D. Vanderbilt, *Phys. Rev. B* **41**, 7892 (1990).

¹³G. Kresse and J. Furthmüller, *Phys. Rev. B* **54**, 11169 (1996).

¹⁴G. Kresse and D. Joubert, *Phys. Rev. B* **59**, 1758 (1999).

¹⁵R. F. W. Bader, *Atoms in Molecules: A Quantum Theory* (Oxford University Press, Oxford, 1990).

- ¹⁶J. I. Rodríguez, P. W. Ayers, A. W. Götz, and F. L. Castillo-Alvarado, *J. Chem. Phys.* **131**, 021101 (2009).
- ¹⁷R. M. Martin, *Electronic Structure: Basic Theory and Practical Methods* (Cambridge University Press, Cambridge, 2004).
- ¹⁸J. P. Perdew, K. Burke, and M. Ernzerhof, *Phys. Rev. Lett.* **77**, 3865 (1996).
- ¹⁹J. P. Perdew and Y. Wang, *Phys. Rev. B* **45**, 13244 (1992).
- ²⁰A. D. Becke, *Phys. Rev. A* **38**, 3098 (1988).
- ²¹J. C. Slater, *Phys. Rev.* **51**, 846 (1937).
- ²²M. Yu and D. R. Trinkle, *J. Chem. Phys.* **134**, 064111 (2011).
- ²³H. J. Monkhorst and J. D. Pack, *Phys. Rev. B* **13**, 5188 (1976).
- ²⁴N. Moll, A. Kley, E. Pehlke, and M. Scheffler, *Phys. Rev. B* **54**, 8844 (1996).
- ²⁵G. X. Qian, R. M. Martin, and D. J. Chadi, *Phys. Rev. B* **37**, 1303 (1988).
- ²⁶R. Choudhury, D. R. Bowler, and M. J. Gillan, *J. Phys. Condens. Matter* **20**, 235227 (2008).
- ²⁷C. Messmer and J. C. Bilello, *J. Appl. Phys.* **52**, 4623 (1981).
- ²⁸A. F. Wright, *Phys. Rev. B* **74**, 165116 (2006).
- ²⁹M. J. Puska, S. Pöykkö, M. Pesola, and R. M. Nieminen, *Phys. Rev. B* **58**, 1318 (1998).
- ³⁰S. Dannefaer, P. Mascher, and D. Kerr, *Phys. Rev. Lett.* **56**, 2195 (1986).
- ³¹E. O. Kane, *Phys. Rev. B* **31**, 5199 (1985).
- ³²H. L. McMurry, A. W. Solbrig Jr., and J. K. Boyter, *J. Phys. Chem. Solids* **28**, 2359 (1967).
- ³³M. Methfessel and A. T. Paxton, *Phys. Rev. B* **40**, 3616 (1989).
- ³⁴V. Zólyomi, L. Vitos, S. K. Kwon, and J. Kollár, *J. Phys. Condens. Matter* **21**, 095007 (2009).
- ³⁵R. M. Wood, *Proc. Phys. Soc.* **80**, 783 (1962).
- ³⁶R. G. Hennig, D. R. Trinkle, J. Bouchet, S. G. Srinivasan, R. C. Albers, and J. W. Wilkins, *Nat. Mater.* **4**, 129 (2005).
- ³⁷R. J. Weiss, *Philos. Mag.* **27**, 1461 (1973).
- ³⁸O. Jepsen, *Phys. Rev. B* **12**, 2988 (1975).